A two-layer elastic strip under transverse impact loading: analytical solution, finite element, and finite volume simulations

V. Adámek[a], A. Berezovski[b,c], M. Mračko[c], R. Kolman[c,*]

[a] *NTIS - New Technologies for the Information Society, Faculty of Applied Sciences, University of West Bohemia, Technická 8, 301 00 Pilsen, Czech Republic*
[b] *Department of Cybernetics, School of Science, Tallinn University of Technology, Akadeemia 21, 12618 Tallinn, Estonia*
[c] *Institute of Thermomechanics, v.v.i., The Czech Academy of Sciences, Dolejškova 1402/5, 182 00 Praha 8, Czech Republic*

Abstract

In this paper, wave propagation in a two-layer composite strip is investigated analytically and numerically. The strip is loaded by a very short transverse stress pulse. Three cases of the strip problem are assumed: (i) isotropic aluminum Al strip and two-layer strips made of (ii) Al and the ceramics Al_2O_3 and (iii) the ceramics Al_2O_3 and Al. The analytical method is based on Laplace and Fourier transform. The in-house finite element algorithm and thermodynamic consistent finite volume scheme are employed for computations, while the explicit time stepping procedure is used in both cases. The comparison of analytical and numerical results determines the degree of the accuracy of calculations, which is important for simulation of complex wave propagation problems in general heterogeneous media.

Keywords: wave propagation, heterogeneous solids, analytical solution, finite element method, finite volume method, plane stress problem

*Corresponding author
Email addresses: vadamek@kme.zcu.cz (V. Adámek), Arkadi.Berezovski@cs.ioc.ee (A. Berezovski), mracko@it.cas.cz (M. Mračko), kolman@it.cas.cz (R. Kolman)

1. Introduction

Application of elastic wave propagation to inspect the state of real structures and their damage localization is an essential part of structural health monitoring [1]. For instance, acoustic emission testing is completely based on elastic wave phenomena [2]. The acoustic emission testing is the broadly accepted approach for the localization of defects in structures [3–5]. The validity of this approach has, however, certain limitations [6]. In fact, the signal arrival time measurement is performed under the assumption that the propagation velocity is constant in all directions (see, e.g., MISTRAS Acousto-Ultrasonics, https://www.mistrasgroup.com/products/technologies/acousto-ultrasonics.aspx). The wave propagation from a source to the sensor is supposed to be straight and uninterrupted. These assumptions can be invalid due to various possible inhomogeneity effects that can reduce the accuracy of this technique.

This is only one reason to have effective tools for the prediction of wave propagation in real materials and structures. A key element in wave controlling is the prediction of the wavefield for any composite with arbitrarily distributed scatterers of irregular shapes and sizes. It should be noted that classical works in wave propagation [7–9] deal with the theoretical description of propagation, reflection, and transmission of elastic waves in simplified situations. More recent works [10–14] demonstrate the applicability of numerical methods to characterize wave propagation in inhomogeneous materials and structures.

This means that if the geometry of inhomogeneities and material properties of constituents are prescribed, then the only problem is in the accuracy of calculations. The accuracy is determined by the comparison of an approximate numerical solution with the true analytical one. However, analytical solutions are usually known for idealized isotropic homogeneous materials and simplified geometry.

It is a great advantage of the paper that the analytical solution can be constructed for the dynamic transverse load of a two-layer infinite strip following [15]. Having an analytical solution, its comparison with numerical solutions can be performed. In the paper, calculations by the finite element method and by the finite volume method are compared with the analytical solution to examine their accuracy on the example of a two-layer strip under dynamic transverse loading. The paper is a continuation of the work performed on one-dimensional wave propagation in layered bars [16].

2. Problem description

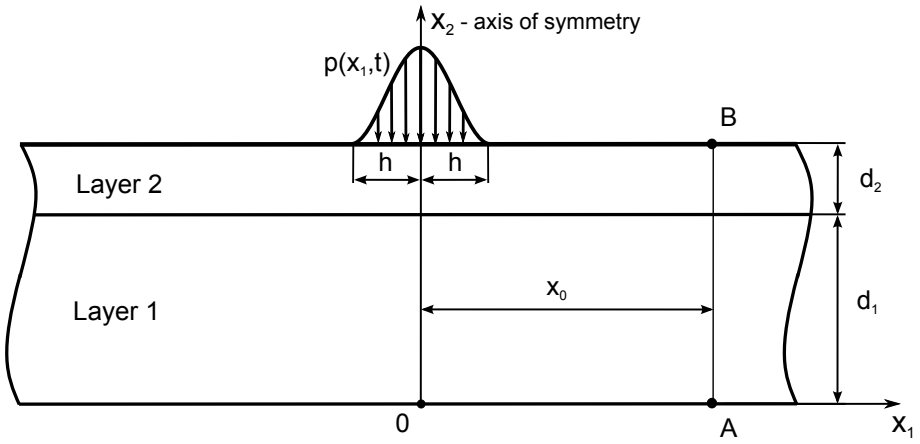

Figure 1: Sketch of the problem.

We will consider the transient response of a two-layer elastic strip to the transverse impulse loading. The sketch of the problem is shown in Fig. 1. The infinite elastic strip is composed of two homogeneous isotropic layers of different materials. Namely, the bottom layer 1 of the thickness $d_1 = 30\,\mathrm{mm}$ is made from aluminum Al and the upper layer 2 of the thickness $d_2 = 10\,\mathrm{mm}$ is made from aluminum oxide Al_2O_3 (ceramics). The properties of materials are given in Table 1. The corresponding longitudinal and shear wave speeds are also stated there. The values of longitudinal speed c_p in parenthesis correspond to plane stress conditions. It is clear from the values specified in Table 1 that the composite strip is made from two materials with highly different properties.

Material	Density $\rho\,[kg/m^3]$	Young modulus $E\,[GPa]$	Poisson ratio ν	Longitudinal wave speed $c_p\,[m/s]$	Shear speed $c_s\,[m/s]$	Source
Al	2700	70.6	0.345	6420 (5448)	3040	[17]
Al_2O_3	3970	401	0.24	10911.2 (10352.8)	6381.9	[18]

Table 1: Values of material properties.

Initially, the strip is at rest. The stress loading $p(x_1, t)$, as normal pressure, is nonzero only for $x_2 = d_1 + d_2$ and for $x_1 \in [-h, h]$. All other parts of the strip boundaries were stress-free. The shape of the loading $p(x_1, t)$ is a

smooth cosine pulse of duration t_0 with the amplitude σ_0 changing according to cosine function in x_1, namely,

$$p(x_1, t) = \frac{\sigma_0}{2} \cos\left(\frac{\pi}{2}\frac{x_1}{h}\right)\left(1 - \cos\frac{2\pi t}{t_0}\right)[H(t) - H(t - t_0)], \tag{1}$$

where $H(t)$ denotes the Heaviside step function. Corresponding parameters contained in (1) were the following: $h = 2\,\mathrm{mm}$, $\sigma_0 = 10^6\,\mathrm{Pa}, t_0 = 2 \cdot 10^{-6}\,\mathrm{s}$.

3. Governing equations

In this section, basic equations of dynamic problems in solids are specified for 2D case under plane stress conditions. Let $\Omega \subset \mathbb{R}^3$ be an open, bounded domain with a piecewise smooth boundary $\partial\Omega$ and $t \in [0, T]$ is the time range of interest. Neglecting both geometrical and physical nonlinearities, we can write the bulk equations (balance of linear momentum) of homogeneous linear isotropic elasticity in the absence of body forces as follows [19]:

$$\rho\frac{\partial v_i}{\partial t} = \frac{\partial \sigma_{ij}}{\partial x_j}, \quad \text{on} \quad \Omega \times [0, T]. \tag{2}$$

The balance of linear momentum is complemented by the Hooke law in the form

$$\frac{\partial \sigma_{ij}}{\partial t} = \lambda\frac{\partial v_k}{\partial x_k}\delta_{ij} + \mu\left(\frac{\partial v_i}{\partial x_j} + \frac{\partial v_j}{\partial x_i}\right), \tag{3}$$

where t is time, x_i are spatial coordinates, v_i are the velocity components, σ_{ij} denotes the Cauchy stress tensor, ρ is the density, λ and μ are the Lamé coefficients given by $\lambda = E\nu/((1+\nu)(1-2\nu))$ and $\mu = E/(2(1+\nu))$, E is the Young modulus and ν is the Poisson ratio. We assume that E and ν could be different at each material point.

Since initially the strip is at rest, therefore the initial displacement and velocity fields are of zero values. The Neumann boundary conditions are assumed as the pressure at the boundary $\Gamma_N = [-h, h] \times [x_2 = d_1 + d_2]$ with the space distribution and time history given by Eq. (1). The strip is floating in the space, therefore the Dirichlet boundary conditions is not taken into account.

3.1. Plane stress approximation

For the 2D problem, in our case of the strip geometry, we have $\Omega = (-\infty, \infty) \times [0, d_1 + d_2]$. The strip is supposed to be thin along the x_3 direction then stresses on all parallel x_3-planes are sufficiently small and can be neglected, i.e.,

$$\sigma_{i3} = 0, \quad i = 1, 2, 3. \tag{4}$$

This approximation is called plane stress approximation. Though the displacement u_3 in the direction of x_3 does not vanish, the others (u_1, u_2) are independent of the coordinate x_3; that is,

$$u_i = u_i(x_1, x_2), \quad i = 1, 2. \tag{5}$$

It follows that the strain tensor components, ε_{i3}, are

$$\varepsilon_{i3} = 0, \quad \varepsilon_{33} = -\frac{\nu}{E}\sigma_{ii}, \quad i = 1, 2. \tag{6}$$

Equations of motion (2)-(3) specialized to plane stress conditions have the form

$$\rho\frac{\partial v_1}{\partial t} = \frac{\partial \sigma_{11}}{\partial x_1} + \frac{\partial \sigma_{12}}{\partial x_2}, \tag{7}$$

$$\rho\frac{\partial v_2}{\partial t} = \frac{\partial \sigma_{21}}{\partial x_1} + \frac{\partial \sigma_{22}}{\partial x_2}. \tag{8}$$

Accordingly, strain-velocity relationships are represented as

$$\frac{\partial \varepsilon_{11}}{\partial t} = \frac{\partial v_1}{\partial x_1}, \tag{9}$$

$$\frac{\partial \varepsilon_{12}}{\partial t} = \frac{1}{2}\left(\frac{\partial v_1}{\partial x_2} + \frac{\partial v_2}{\partial x_1}\right), \tag{10}$$

$$\frac{\partial \varepsilon_{22}}{\partial t} = \frac{\partial v_2}{\partial x_2}. \tag{11}$$

3.2. Stress-strain relation

Stress-strain relations (the Hooke law) which close the system of governing equations under plane stress conditions have the form

$$\sigma_{11} = (\overline{\lambda} + 2\mu)\varepsilon_{11} + \overline{\lambda}\varepsilon_{22}, \tag{12}$$

$$\sigma_{12} = \sigma_{21} = 2\mu\varepsilon_{12}, \tag{13}$$

$$\sigma_{22} = (\overline{\lambda} + 2\mu)\varepsilon_{22} + \overline{\lambda}\varepsilon_{11}, \tag{14}$$

where $\overline{\lambda} = 2\mu\lambda/(\lambda + 2\mu)$. Time derivatives of the stress-strain relations together with compatibility conditions determine relationships

$$\frac{\partial\sigma_{11}}{\partial t} = (\overline{\lambda} + 2\mu)\frac{\partial v_1}{\partial x_1} + \overline{\lambda}\frac{\partial v_2}{\partial x_2}, \tag{15}$$

$$\frac{\partial\sigma_{22}}{\partial t} = \overline{\lambda}\frac{\partial v_1}{\partial x_1} + (\overline{\lambda} + 2\mu)\frac{\partial v_2}{\partial x_2}, \tag{16}$$

$$\frac{\partial\sigma_{12}}{\partial t} = \frac{\partial\sigma_{21}}{\partial t} = \mu\left(\frac{\partial v_1}{\partial x_2} + \frac{\partial v_2}{\partial x_1}\right). \tag{17}$$

These equations together with the balance of linear momentum (7)–(8) form the system of equations, which is convenient for the solution.

3.3. Wave speeds

The wave speeds under plane stress conditions are specified for the isotropic case as

$$c_p = \sqrt{\frac{E}{(1-\nu^2)\,\rho}}, \qquad c_s = \sqrt{\mu/\rho}. \tag{18}$$

In the case of heterogeneous media, material parameters depend on position of material points.

4. Analytical solution

In this Section, we set out the technique used for obtaining the analytical solution of the studied problem.

4.1. Derivation procedure and final formulas for transforms of stress components

To find the analytical solution of the problem formulated in Sections 2 and 3, it is advantageous to introduce a local coordinate system $x_{1,L} - x_{2,L}$ for each Lth layer ($L = 1, 2$). The origins of these systems are localized in the geometrical centres of layers, i.e., the domain of the Lth layer are defined as $(-\infty, +\infty) \times [-d_L/2, d_L/2]$. Then one can use a procedure for the derivation of desired formulas of stress components similar to that employed in

[15]. Taking the Laplace transform in time domain, we transfer the original systems of equations of motion for each layer to spatial boundary value problems with a complex parameter p. The general solutions of obtained systems can then be expressed by means of Fourier integrals. Taking into account the symmetry of the problem, the Laplace transforms of all non-zero stress components denoted hereinafter by a hat are given for $\omega \in \mathbb{R}$ by Fourier integrals having the form

$$\hat{\sigma}_{11,L}(x_{1,L}, x_{2,L}, p) = \frac{1}{\pi}\int_0^\infty [(A_{1,L}\sinh(x_{2,L}\lambda_{1,L}) + A_{2,L}\cosh(x_{2,L}\lambda_{1,L}))\, k_{1,L} - \\ - (A_{3,L}\sinh(x_{2,L}\lambda_{2,L}) + A_{4,L}\cosh(x_{2,L}\lambda_{2,L}))\, k_{2,L}]\cos(\omega x_{1,L})d\omega\,, \tag{19}$$

$$\hat{\sigma}_{22,L}(x_{1,L}, x_{2,L}, p) = \frac{1}{\pi}\int_0^\infty [(A_{1,L}\sinh(x_{2,L}\lambda_{1,L}) + A_{2,L}\cosh(x_{2,L}\lambda_{1,L}))\, k_{3,L} + \\ + (A_{3,L}\sinh(x_{2,L}\lambda_{2,L}) + A_{4,L}\cosh(x_{2,L}\lambda_{2,L}))\, k_{2,L}]\cos(\omega x_{1,L})d\omega\,, \tag{20}$$

$$\hat{\sigma}_{12,L}(x_{1,L}, x_{2,L}, p) = -\frac{1}{\pi}\int_0^\infty [(A_{1,L}\cosh(x_{2,L}\lambda_{1,L}) + A_{2,L}\sinh(x_{2,L}\lambda_{1,L}))\, k_{4,L} + \\ + (A_{3,L}\cosh(x_{2,L}\lambda_{2,L}) + A_{4,L}\sinh(x_{2,L}\lambda_{2,L}))\, k_{5,L}]\sin(\omega x_{1,L})d\omega\,. \tag{21}$$

The complex functions involved in (19) - (21) are introduced by the following relations

$$\lambda_{1,L} = \omega\sqrt{1+\frac{p^2}{\omega^2 c_{p,L}^2}}\,, \quad \lambda_{2,L} = \omega\sqrt{1+\frac{p^2}{\omega^2 c_{s,L}^2}}\,, \quad k_{1,L} = \frac{E_L\nu_L}{1-\nu_L^2} - \frac{2G_L c_{p,L}^2\omega^2}{p^2}\,, \\ k_{2,L} = \frac{4G_L c_{s,L}^2\lambda_{2,L}\omega}{p^2}\,, \quad k_{3,L} = 2\left(\frac{\omega^2 c_{p,L}^2}{p^2}+1\right)G_L + \frac{E_L\nu_L}{1-\nu_L^2}, \\ k_{4,L} = \frac{2G_L c_{p,L}^2\lambda_{1,L}\omega}{p^2}\,, \quad k_{5,L} = 2\left(\frac{2c_{s,L}^2\omega^2}{p^2}+1\right)G_L\,, \tag{22}$$

where G_L denotes the shear modulus of the material in the Lth layer ($L = 1, 2$) and $A_{i,L} = A_{i,L}(\omega, p)$ for $i = 1\ldots 4$ and $L = 1, 2$ represent 8 unknown

complex functions which need to be found using the Laplace transform of four boundary conditions of the problem and four conditions defined at the interface of the strip layers. Following the problem description given in Section 2, the Laplace transforms of mentioned conditions can be written as (in order from the upper edge of the strip)

$$\begin{gathered}
\hat{\sigma}_{22,2}(x_{1,2}, d_2/2, p) = \hat{p}(x_{1,2}, p)\,, \quad \hat{\sigma}_{12,2}(x_{1,2}, d_2/2, p) = 0\,, \\
\hat{u}_{1,1}(x_{1,1}, d_1/2, p) = \hat{u}_{1,2}(x_{1,2}, -d_2/2, p)\,, \quad \hat{u}_{2,1}(x_{1,1}, d_1/2, p) = \hat{u}_{2,2}(x_{1,2}, -d_2/2, p)\,, \\
\hat{\sigma}_{22,1}(x_{1,1}, d_1/2, p) = \hat{\sigma}_{22,2}(x_{1,2}, -d_2/2, p)\,, \quad \hat{\sigma}_{12,1}(x_{1,1}, d_1/2, p) = \hat{\sigma}_{12,2}(x_{1,2}, -d_2/2, p)\,, \\
\hat{\sigma}_{22,1}(x_{1,1}, -d_1/2, p) = 0\,, \quad \hat{\sigma}_{12,1}(x_{1,1}, -d_1/2, p) = 0\,.
\end{gathered} \tag{23}$$

4.2. Evaluation process and its precision

The evaluation process of derived relationships (19) - (21) is realized in two basic steps. Namely, these are the Fourier integrals evaluation (FIE) and the inverse Laplace transform. The sequence of these steps may also be interchanged due to the properties of the integrands in Eqs. (19) - (21). The first mentioned step was managed by using the standard numerical Simpson rule with a constant integration step in this work. The second step has been resolved by means of an algorithm for numerical inverse Laplace transform (NILT). Specifically, the procedure based on FFT and Wynn's epsilon algorithm was used (see [20] and [21] for more details).

Although the derived relationships (19) - (21) are exact, it is obvious that their evaluation will suffer from numerical errors. The errors are caused not only by two numerical procedures mentioned above but also by the precision limits of the software used for the evaluation. In this work, a Matlab code with double precision arithmetics has been used. This limitation may come into play when the hyperbolic functions contained in the integrands of derived Laplace transforms need to be evaluated for large arguments, i.e., for large values of the variable ω of the Fourier integrals. The same concerns to the functions $A_{i,L}(\omega, p)$ evaluated from formulas which can be derived exactly in this case of two-layer strip. These issues can be overcome by symbolic calculations of higher precision but it is always redeemed by significantly higher demands on computational time.

The precision of the algorithm used for NILT is discussed in detail in [22]. We focus on the accuracy of FIE process here. Even though there exist very sophisticated algorithms for numerical integration, we used the simple

straightforward Simpson rule with constant integration step, as mentioned above. This decision resulted from the analysis of integrands appearing in Eqs. (19) - (21) after the NILT process. As expected, the precision of FIE is principally influenced by the integration step $d\omega$ and by the upper limit of integration ω_{max}. Their right choice is predetermined by the behavior of integrands depending on t, x_1 and x_2.

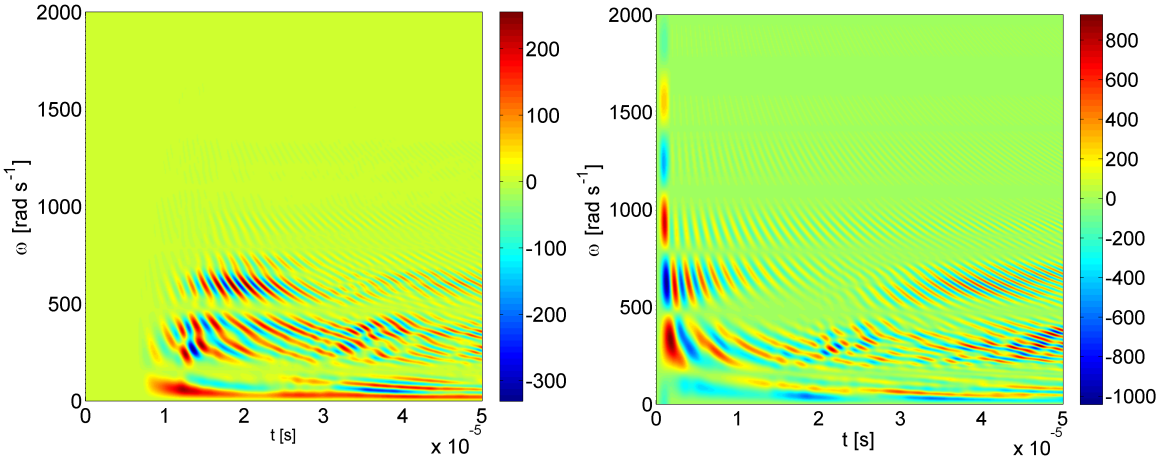

Figure 2: The dependence of σ_{11} integrand in $[Pa{\cdot}s]$ on t and ω: (a) point A, (b) point B

We focus on t and x_2 dependence first. For this purpose, we assume the strip mentioned in Section 2, i.e., the strip composed of 30 mm of Al (1st layer) and of 10 mm of Al_2O_3 (2nd layer). The dependencies of σ_{11} integrand on $t \in [0, 50]$ μs and $\omega \in [0, 2000]$ rad s^{-1} are shown for studied points A and B for $x_0 = 10$ mm (i.e., for different values of x_2) in Fig. 2(a) and Fig. 2(b), respectively. It is obvious that contrary to the point A, the calculation of the response at point B ($x_2 = 40$ mm) for very short times requires $\omega_{max} > 2000$ to take into account the integrand oscillations. On the other hand, to obtain good results for longer times, the values of ω_{max} can be reduced to about 2000 rad s^{-1} at both studied points, i.e., both for $x_2 = 0$ mm and $x_2 = 40$ mm.

The specific character of σ_{11} integrand oscillations at point A is obvious from Fig. 3. The curves presented in this figure correspond to vertical cuts of Fig. 2(a) at times $t \doteq 10$ μs and $t = 50$ μs. Such oscillations then determine the size of the integration step $d\omega$. It is clear that calculations for larger values of t require smaller $d\omega$. Similar dependence of $d\omega$ on x_1

can be deduced from Eqs. (19) - (21). Since the variables $x_{1,L}$ appear after the NILT process still in the argument of sin or cos functions, the size of $d\omega$ needs to be reduced with increasing x_1.

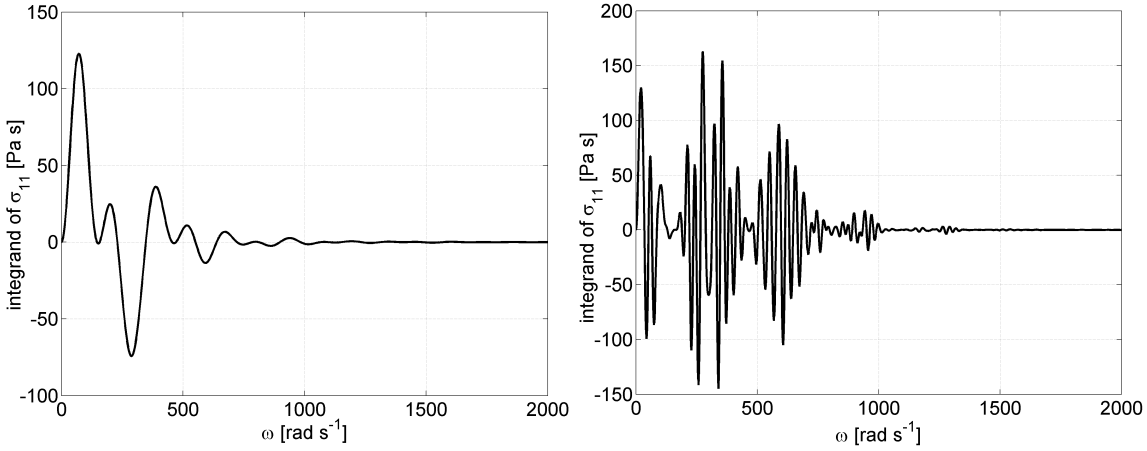

Figure 3: The dependence of σ_{11} integrand at point A on ω at specific times: (a) $t \doteq 10$ μs, (b) $t = 50$ μs

It is clear from the previous discussion that the evaluation of Eqs. (19) - (21) is loaded by numerical errors. But if the applied numerical approaches are used wisely, very precise results can be obtained. Their precision can then be verified by means of the exact arrival times of P-waves to the points of interest. In the case of studied points A and B and the Al–Al_2O_3 strip, these times can be calculated as

$$t_A = \frac{1}{c_{p,Al_2O_3}}\sqrt{d_2^2 + \left[\frac{(x_0-h)d_2}{d_1+d_2}\right]^2} + \frac{1}{c_{p,Al}}\sqrt{d_1^2 + \left[\frac{(x_0-h)d_1}{d_1+d_2}\right]^2} \doteq 6.601 \ \mu\text{s}\,,$$
$$t_B = \frac{x_0-h}{c_{p,Al_2O_3}} \doteq 0.7727 \ \mu\text{s}. \tag{24}$$

If we make a detailed view of $\sigma_{11}(t)$ at mentioned points, then we find out that the arrival times obtained from the evaluated solution are in very good agreement with the theoretical ones given by Eq. (24). It is clearly visible from Fig. 4 where the stress component σ_{11} at points A and B is shown. The times t_A and t_B are highlighted by vertical dotted lines. Naturally, if

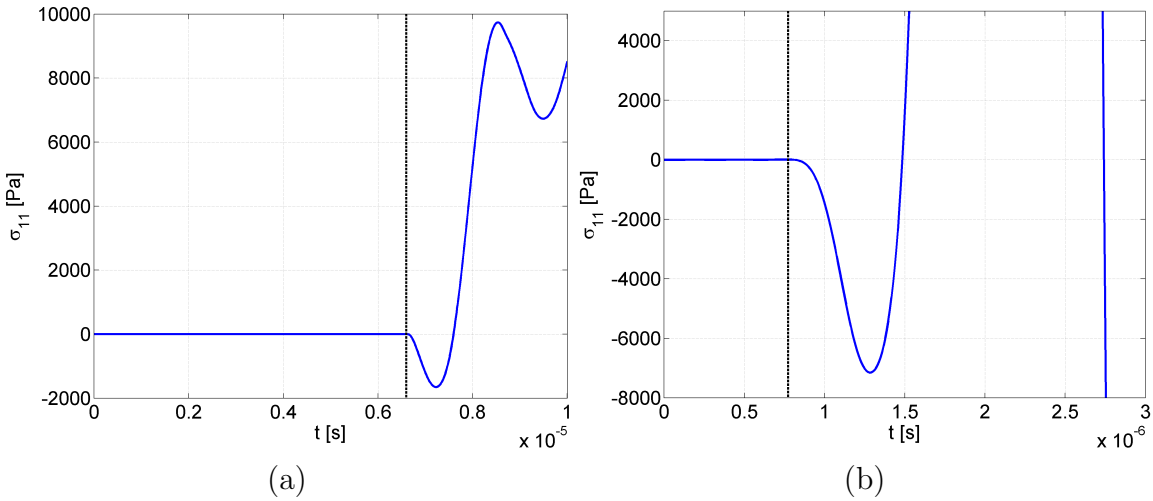

Figure 4: The detailed views of $\sigma_{11}(t)$ with times of P-wave arrivals to (a) point A and (b) point B.

one makes a detailed inspection of σ_{11} values calculated at points A and B at times $t < t_A$ and $t < t_B$, respectively, then the values are not exactly equal to zero. The differences from the zero value are more than four (nearly six) orders smaller in magnitude than the maximal values of σ_{11} at point A (point B) on the time interval $[0, 50]$ μs. It is evident that the results of such precision can be used for the validation of numerical results in the following sections.

5. Finite element procedure with explicit time integration

5.1. Weak formulation and spatial discretization

As the first step, we rewrite the equation of motion (2) in terms of displacements u_i

$$\rho \frac{\partial^2 u_i}{\partial t^2} = \frac{\partial \sigma_{ij}}{\partial x_j}. \tag{25}$$

Next, we represent equation of motion (25) in the weak form by multiplying it by a virtual field $\delta\varphi_i$ and integrating over the domain Ω using Green's theorem

$$\int_\Omega \rho \frac{\partial^2 u_i}{\partial t^2} \delta\varphi_i \, d\Omega + \int_\Omega C_{ijkl} \frac{\partial u_k}{\partial x_l} \frac{\partial \delta\varphi_i}{\partial x_j} \, d\Omega = \int_{\partial\Omega} t_i^* \delta\varphi_i \, dS, \tag{26}$$

with a general stress-strain law $\sigma_{ij} = C_{ijkl}\varepsilon_{kl}$ and the traction t_i^* at the boundary $\partial\Omega$.

Applying a spatial discretization

$$u_i = \sum_{a=1}^{n} N^a q_i^a, \quad \delta\varphi_i = \sum_{a=1}^{n} N^a \delta\varphi_i^a, \tag{27}$$

we end up with

$$\int_\Omega \rho N^b N^a \frac{\partial^2 q_i^b}{\partial t^2} \delta\varphi_i^a \, d\Omega + \int_\Omega C_{ijkl} \frac{\partial N^b}{\partial x_l} \frac{\partial N^a}{\partial x_j} q_k^b \delta\varphi_i^a \, d\Omega = \int_{\partial\Omega} t_i^* N^a \delta\varphi_i^a \, dS. \tag{28}$$

Due to the arbitrariness of the virtual field $\delta\varphi_i$, we can represent the latter relationship in the matrix form

$$\mathbf{M}\ddot{\mathbf{q}}(t) + \mathbf{K}\mathbf{q}(t) = \mathbf{f}_{ext}(t), \tag{29}$$

where $\mathbf{q}(t)$ is the nodal displacement vector, $\ddot{\mathbf{q}}(t)$ is the nodal acceleration vector, $\mathbf{M}$ is the mass matrix having the form

$$\mathbf{M} = \int_\Omega \rho \mathbf{N}^{\mathrm{T}} \mathbf{N} \, d\Omega, \tag{30}$$

$\mathbf{K}$ is the stiffness matrix

$$\mathbf{K} = \int_\Omega \mathbf{B}^{\mathrm{T}} \mathbf{C} \mathbf{B} \, d\Omega \tag{31}$$

and $\mathbf{f}_{ext}$ is the load vector

$$\mathbf{f}_{ext} = \int_{\Gamma_N} \mathbf{N}^T \mathbf{t}^* \, d\Gamma. \tag{32}$$

In linear elastodynamic problems, the matrices $\mathbf{K}$ and $\mathbf{M}$ are constant for each finite element but may differ for distinct elements due to heterogeneous media. $\mathbf{C}$ is the elasticity matrix, $\mathbf{B}$ is the strain-displacement matrix, $\mathbf{N}$ stores the displacement interpolation functions, for details see [23].

For the finite element simulation, we use the standard finite element based on displacement formulation with linear shape functions [23]. The integrals in Eqs. (30)-(32) are evaluated by the Gauss integration procedure. To reduce the integration cost for $\mathbf{K}$, we use the one-point integration

rule with the hourglass control as described in [24]. Elements stiffness matrix $\mathbf{K}_{el}^{1gp}$ obtained by the one-point Gauss integration are complemented by a stabilization stiffness matrix $\mathbf{K}_{stab}$ suppressing hourglass modes, i.e., $\mathbf{K}_{el} = \mathbf{K}_{el}^{1gp} + \mathbf{K}_{stab}$. The mass matrix $\mathbf{M}$ is lumped using row-summing procedure [23], which is preferred in the explicit time integration due to temporal-spatial dispersion [25].

5.2. Explicit time integration in FEM

In this paper, we use the central difference (CD) scheme for explicit time integration as described in the book [26]. The update of nodal velocities at each time step is then split into two half-steps, and the desired values of velocities can be prescribed directly. This approach is also called *leapfrog* integration. It is assumed that quantities $\mathbf{q}(t), \dot{\mathbf{q}}(t), \ddot{\mathbf{q}}(t)$ are known at the time instant t, and the task is to find their values at the next time step $t+\Delta t$. The central difference scheme as the leapfrog integration procedure takes the form presented in Algorithm 1:

Initialize $t^0 = 0$, $\mathbf{q^0}$, $\dot{\mathbf{q}}^0$, assemble $\mathbf{M}$, $\mathbf{K}$, and compute
$\ddot{\mathbf{q}}^0 = \mathbf{M}^{-1}\left(\mathbf{f}_{ext}^0 - \mathbf{K}\mathbf{q}^0\right)$
while $t < T$ **do**
  setting of the time step size Δt
  $\dot{\mathbf{q}}(t + \frac{\Delta t}{2}) = \dot{\mathbf{q}}(t) + \ddot{\mathbf{q}}(t)\frac{\Delta t}{2}$;
  $\mathbf{q}(t + \Delta t) = \mathbf{q}(t) + \dot{\mathbf{q}}(t + \frac{\Delta t}{2})\Delta t$;
  application of boundary conditions;
  $\mathbf{r}(t + \Delta t) = \mathbf{f}_{ext}(t + \Delta t) - \mathbf{K}\mathbf{q}(t + \Delta t)$;
  $\ddot{\mathbf{q}}(t + \Delta t) = \mathbf{M}^{-1}\mathbf{r}(t + \Delta t)$;
  $\dot{\mathbf{q}}(t + \Delta t) = \dot{\mathbf{q}}(t + \frac{\Delta t}{2}) + \ddot{\mathbf{q}}(t + \Delta t)\frac{\Delta t}{2}$;
  application of boundary conditions;
  $t = t + \Delta t$;
end

Algorithm 1: The central difference scheme in the *leapfrog* form for direct time integration of elastodynamic problems

It should be noted that the presented scheme is conditionally stable [23]. This means that the value of the time step Δt has to satisfy the stability limit $\Delta t < \Delta t_{cr}$, where Δt_{cr} is the critical limit given as $\Delta t_{cr} = 2/\omega_{max}$. Here ω_{max} is the maximum angular frequency of the discretized homogeneous system (29). It is known that the maximum eigenfrequency of the assembled finite element mesh is smaller than the maximum value of each separated finite element consisted in the mesh [23], because this value is taken as a

maximum over all values as $\omega_{max} \approx max(\omega^e_{max})$. Here $\omega^e_{max} = 2c^e_p/h^e$ is the maximum frequency of separated element with longitudinal wave speed c^e_p and length h_e for the case of the lumped mass matrix for regular meshes.

A regular mesh is preferred due to dispersion in the wave propagation problem. Suitable Dirichlet and Neumann boundary conditions and initial conditions should be included for solving the problem. Dirichlet boundary conditions are applied directly to nodal values of the displacement vector, velocity vector, acceleration vector, respectively, at Γ_D. Neumann boundary conditions are applied through the external nodal force $\mathbf{f}_{ext}(t)$. In the case of stress-free boundary conditions, the nodal external force vector is zero for material points at the boundary. It is known that Neumann boundary condition is only an approximation and goes to exact values as convergence properties of FEM with decreasing mesh size. The final results of stress tensor $\sigma_{\mathbf{ij}}$, computed at integration points inside the finite element domain, are interpolated into the nodal values. This technique is called stress recovering. In the paper, we use the ZZ (Zienkiewicz and Zhu) algorithm for the stress recovery [27], which evaluates the stress tensor $\sigma_{\mathbf{ij}}$ values correctly.

6. Finite volume scheme

For finite volume calculation, governing equations (7)–(8) and (15)–(17) are presented in the conservation form [28]

$$\frac{\partial \mathbf{U}}{\partial t} + \frac{\partial \mathbf{F}}{\partial x_1} + \frac{\partial \mathbf{G}}{\partial x_2} = \mathbf{0}, \tag{33}$$

with the vector of variables $\mathbf{U}$ and fluxes $\mathbf{F}$ and $\mathbf{G}$ defined as

$$\mathbf{U} = \begin{pmatrix} \rho v_1 \\ \rho v_2 \\ \sigma_{11} \\ \sigma_{12} \\ \sigma_{22} \end{pmatrix}, \quad \mathbf{F} = \begin{pmatrix} \sigma_{11} \\ \sigma_{12} \\ (\overline{\lambda} + 2\mu) v_1 \\ \mu v_2 \\ \overline{\lambda} v_1 \end{pmatrix}, \quad \mathbf{G} = \begin{pmatrix} \sigma_{12} \\ \sigma_{22} \\ \overline{\lambda} v_2 \\ \mu v_1 \\ (\overline{\lambda} + 2\mu) v_2 \end{pmatrix}. \tag{34}$$

For the discretisation, a regular Cartesian grid of rectangular cells is used in space, and time is discretised by time levels. Variables are approximated by averaged values over cells. The use of cell averages is the standard procedure in the finite-volume method [29, 28]. Integrating the governing equations over the control volume results in the Godunov-type numerical scheme [28]

$$\mathbf{U}^{k+1}_{n,m} = \mathbf{U}^k_{n,m} + \frac{\Delta t}{\Delta x_1} \left(\mathbf{F}^k_{n+1,m} - \mathbf{F}^k_{n,m} \right) + \frac{\Delta t}{\Delta x_2} \left(\mathbf{G}^k_{n,m+1} - \mathbf{G}^k_{n,m} \right). \tag{35}$$

Here the superscript k denotes time level and subscripts n and m indicate the number of cell in horizontal and vertical directions, respectively.

The numerical fluxes $\mathbf{F}^k_{n,m}$ and $\mathbf{G}^k_{n,m}$ are computed by solving Riemann problems at interfaces between cells [29, 28]. Various methods have been proposed for the solution of Riemann problems [30–32, 29]. In the paper, the thermodynamically consistent version of the wave propagation algorithm [33] is applied using jump relations at interfaces between computational cells, which express the continuity of true stresses and velocities. This algorithm provides algebraic procedure for the solution of Riemann problems, second-order accuracy [33], and stability up to values of Courant number close to unity.

6.1. Boundary conditions

To be able to perform the calculation of a particular problem we need to specify initial and boundary conditions. Initial conditions fix the state of each cell at a chosen time instant. We suppose that initially the strip is at rest, which assumes zero values for all wanted fields. Boundary conditions are imposed by means of ghost cells following [29]. At the loaded upper boundary, the value of the normal stress in each cell and at each time step is given in advance. At the stress-free bottom boundary, the value of the normal stress is zero. Lateral boundary conditions are not specified because the length of the strip is chosen such that the influence of these boundaries is absent.

7. Numerical results and comparison with the analytical solution

In this Section, we present the results of numerical solution of pulse propagation in the homogeneous and heterogeneous strip. The results obtained by the in-house finite element algorithm and by the finite volume scheme specified above are compared to the analytical solution. The comparison of non-dimensional stress component σ_{11}/σ_0 is made at two selected points A and B for $x_0 = 10\,\mathrm{mm}$ (see the problem sketch in Fig 1). Note that stress components σ_{22} and σ_{12} have zero values at the points A and B, therefore only the normal stress σ_{11} is of interest.

We start with the homogeneous case and continue with the heterogeneous case of a layered strip composed by two different materials as specified in Section 2.

7.1. Homogeneous aluminum strip

Based on the geometry of the problem shown in Fig. 1, the values of parameters used for the numerical simulations are chosen as follows:

- Loading size $h = 2\,\text{mm} = 10\,\Delta x_1$;
- Strip thickness $d_1 + d_2 = 40\,\text{mm} = 200\,\Delta x_1$;
- Strip length $= 120\,\text{mm} = 600\,\Delta x_2$;
- Space step (mesh size) $\Delta x_1 = \Delta x_2 = 0.2\,\text{mm}$;
- Distance $x_0 = 10\,\text{mm} = 50\Delta x_1$.

The time step Δt for explicit schemes is determined by the maximum of longitudinal velocity in the studied material. For pure aluminum, the value of the longitudinal wave velocity is 5448 m/s (see Table 1), which determines

$$\Delta t = \Delta x_1/c_p = 2 \cdot 10^{-4}/5448 = 3.67 \cdot 10^{-8}\,\text{s}.$$

Correspondingly, the duration of the loafing is

$$t_0 = 200/3.67 = 54\,\Delta t.$$

The characteristic time T_0 is then

$$T_0 = 0.04/5448 = 7.34 \cdot 10^{-6} = 200\,\Delta t.$$

Calculations are performed for 500 time steps providing the absence of influence of lateral boundaries of the strip.

The obtained results are shown in Figs. 5–6. Here blue lines correspond to the analytical solution, red lines represent the finite element simulation, and magenta lines denote results obtained by the finite volume calculations. As one can see, there is almost no difference between the results of finite element computations and the analytical solution.

At the same time, results of the finite volume simulation are qualitatively similar but quantitatively have observable distinctions. The reason is in the imposing of boundary conditions. The finite volume calculations are performed with the value of the Courant number less than unity due to stability demand. Keeping the same size for time and space steps as in the finite element computations, we arrive at the delay in the time variation of

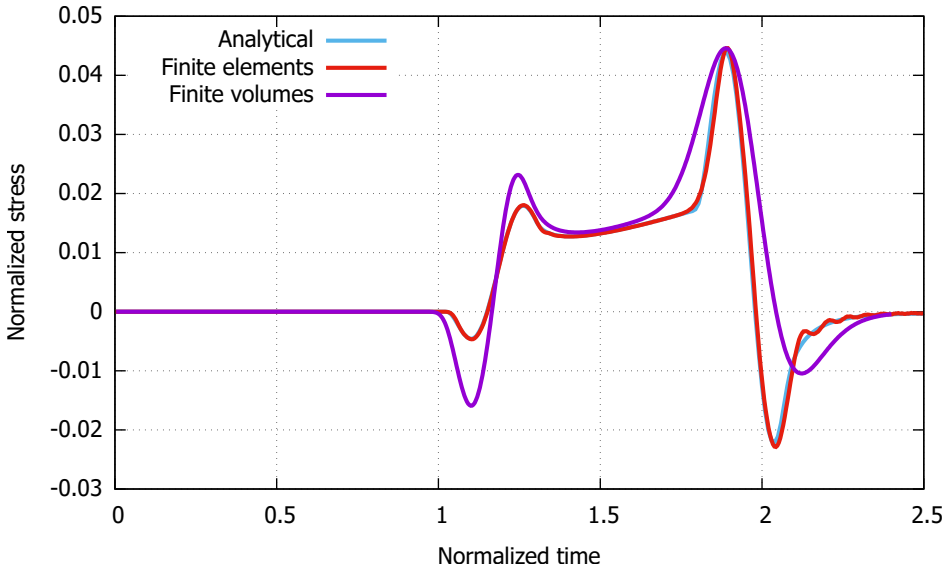

Figure 5: Time history of the normalized stress σ_{11} at point A in homogeneous aluminum strip.

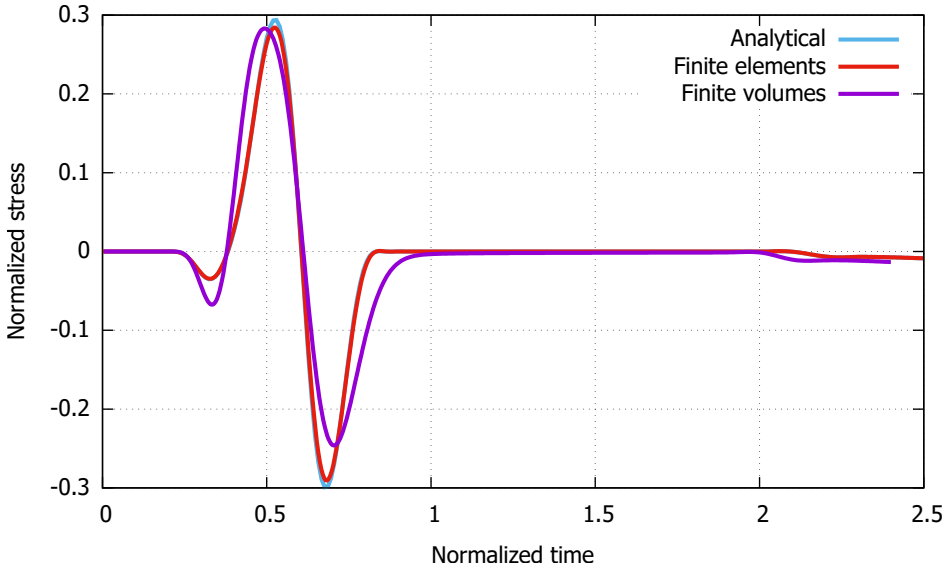

Figure 6: Time history of the normalized stress σ_{11} at point B in homogeneous aluminum strip.

the loading, as it is demonstrated in Fig. 7. Here the blue line corresponds to the value of the Courant number equal to unity used in the finite element solution and the magenta line shows the representation of the same pulse for $Co = 0.83$ employed in the finite volume calculations. The initial delay in input causes the delay in the response.

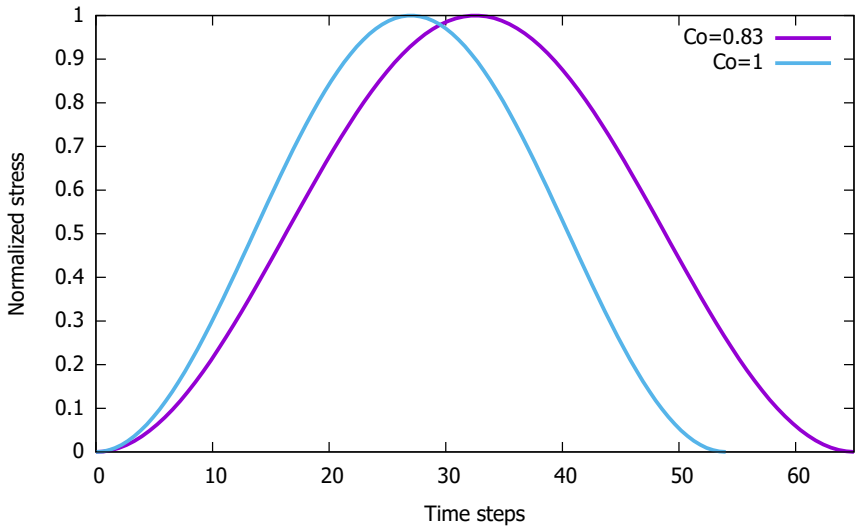

Figure 7: Time variation of loading pulse along the vertical central line.

7.2. Composite strip Al–Al_2O_3

Now we compare the results of numerical simulations with the analytical solution in the case of the layered strip. First, we consider the case where pure aluminum is in the layer 1, and the layer 2 is made from the ceramics Al_2O_3. Since the longitudinal wave speed for Al_2O_3 is 10352.8 m/s, the time step Δt for the simulation is

$$\Delta t = \Delta x / c_p = 2 \cdot 10^{-4} / 10352.8 = 1.93 \cdot 10^{-8}\,\text{s}.$$

Accordingly, the duration of the loafing is

$$t_0 = 200/1.93 = 104\,\Delta t,$$

and the characteristic time T_0 is then

$$T_0 = 0.04/10352.8 = 3.86 \cdot 10^{-6} = 200\,\Delta t.$$

The comparison of numerical and analytical solutions for the time history of the normalized stress σ_{11} at points A and B, in this case, is presented in Figs. 8–9. The finite element and analytical results are practically coincided in the considered case. Even finite volume calculations are closer to analytical and finite element outcomes.

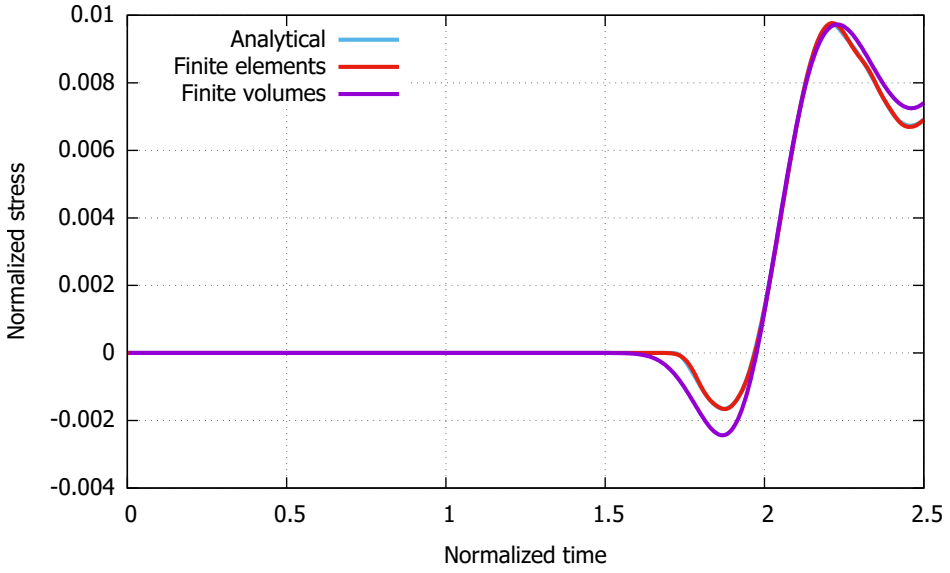

Figure 8: Time history of the normalized stress σ_{11} at point A in two-layer Al–Al_2O_3 strip.

7.3. Composite strip Al_2O_3–Al

Now we alter the placement of the layers to see how this alteration affects the comparison. This means that the layer 1 is made from the ceramic Al_2O_3 and the layer 2 is made from pure aluminum. The parameters used in simulations are the same as in the previous case because the only placement of layers is changed. The comparison of numerical and analytical solutions for the time history of the longitudinal stress at points A and B is presented in Figs. 10–11.

Again, blue lines in mentioned figures still correspond to the analytical solutions, the red ones show the results of finite element computations and the magenta lines denote the results obtained by finite volume calculations.

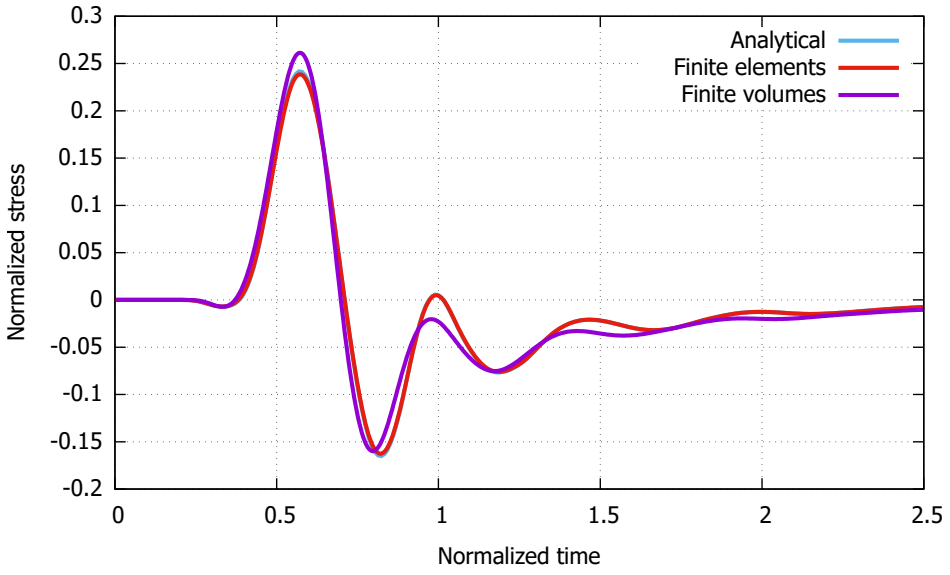

Figure 9: Time history of the normalized stress σ_{11} at point B in two-layer Al–Al_2O_3 strip.

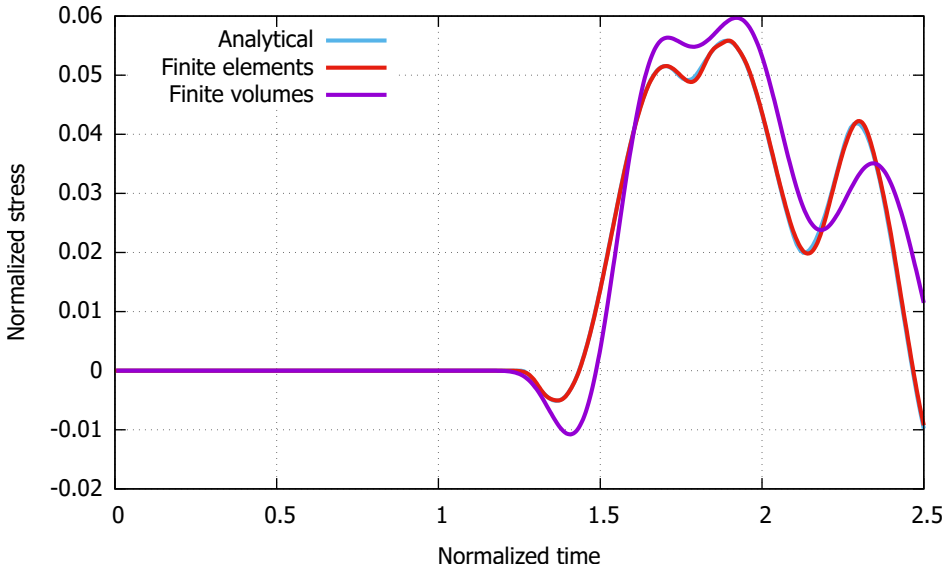

Figure 10: Time history of the longitudinal stress at point A in two-layer Al_2O_3–Al strip.

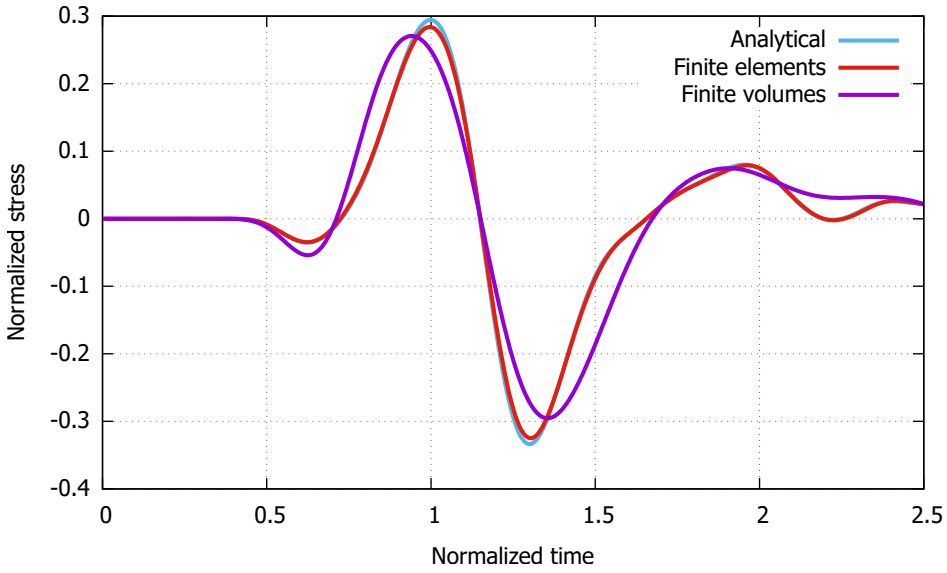

Figure 11: Time history of the longitudinal stress at point B in two-layer Al_2O_3–Al strip.

It is clear that the variation of stresses in time is changed, but finite element results are in a perfect agreement with the analytical ones. As before, finite volume calculations provide less accurate results due to the reasons mentioned above.

8. Conclusions

The main goal of the paper was to examine how accurate are numerical calculations in the comparison with the analytical solution of two-dimensional transverse pulse propagation in a two-layer strip fabricated from materials with highly distinct properties. Time histories of stresses at two different points placed at boundaries of the strip were used for the comparison. It is demonstrated that the in-house finite element algorithm provides the perfect coincidence between analytical and numerical results for all considered examples. The agreement with the results by the finite volume scheme is less definitive due to the distinction in the posing of loading conditions. The main conclusion is that the used numerical algorithms can be applied to the prediction of signal propagation in more complex practical situations.

This work provides the basis for the application of elaborated numerical methods to heterogeneous media with several layers, to graded media, and to media with inclusions. The influence of a microstructure on dispersive behavior of waves in structures can be analyzed by these numerical approaches, where we can control the accuracy. A special attention has to be paid on discontinuous wave propagation in heterogeneous cases which is still an open problem in numerical modeling of composite structures.

Acknowledgements

The research was supported by the Grant project with No. 19-04956S of the Czech Science Foundation (CSF) within institutional support RVO:61388998 (A.B., V.A., R.K.), by the Centre of Excellence for Nonlinear Dynamic Behaviour of Advanced Materials in Engineering CZ.02.1.01/0.0/0.0/15_003/0000493 (Excellent Research Teams) in the framework of Operational Programme Research, Development and Education (M.M.), by Estonian Research Council under Institutional Research Funding IUT33-24 (A.B.) and by the project LO1506 of the Czech Ministry of Education, Youth and Sports under the program NPU I(V.A.).

References

[1] H.-P. Chen, Structural Health Monitoring of Large Civil Engineering Structures, John Wiley & Sons, 2018.

[2] C. U. Grosse, M. Ohtsu, Acoustic Emission Testing, Springer Science & Business Media, 2008.

[3] W. Ostachowicz, P. Malinowski, T. Wandowski, Damage localisation using elastic waves propagation method. Experimental techniques, in: New Trends in Structural Health Monitoring, Springer, 2013, pp. 317–371.

[4] T. Kundu, Acoustic source localization, Ultrasonics 54 (1) (2014) 25–38.

[5] M. E. De Simone, F. Ciampa, S. Boccardi, M. Meo, Impact source localisation in aerospace composite structures, Smart Materials and Structures 26 (12) (2017) 125026.

[6] K. M. Holford, M. J. Eaton, J. J. Hensman, R. Pullin, S. L. Evans, N. Dervilis, K. Worden, A new methodology for automating acoustic emission detection of metallic fatigue fractures in highly demanding aerospace environments: An overview, Progress in Aerospace Sciences 90 (2017) 1–11.

[7] J. Achenbach, Wave Propagation in Elastic Solids, Elsevier, 1973.

[8] K. F. Graff, Wave Motion in Elastic Solids, Clarendon Press, 1975.

[9] A. Nayfeh, Wave Propagation in Layered Anisotropic Media, North Holland, 1995.

[10] J. L. Rose, Ultrasonic Waves in Solid Media, Cambridge University Press, 2004.

[11] H. Aksoy, E. Şenocak, Wave propagation in functionally graded and layered materials, Finite Elements in Analysis and Design 45 (12) (2009) 876–891.

[12] D. G. Aggelis, Wave propagation through engineering materials; assessment and monitoring of structures through non-destructive techniques, Materials and Structures 46 (4) (2013) 519–532.

[13] L. Maio, V. Memmolo, F. Ricci, N. Boffa, E. Monaco, R. Pecora, Ultrasonic wave propagation in composite laminates by numerical simulation, Composite Structures 121 (2015) 64–74.

[14] C. Willberg, S. Duczek, J. Vivar-Perez, Z. Ahmad, Simulation methods for guided wave-based structural health monitoring: a review, Applied Mechanics Reviews 67 (1) (2015) 010803.

[15] V. Adámek, The limits of Timoshenko beam theory applied to impact problems of layered beams, International Journal of Mechanical Sciences 145 (2018) 128–137.

[16] A. Berezovski, R. Kolman, M. Berezovski, D. Gabriel, V. Adámek, Full field computing for elastic pulse dispersion in inhomogeneous bars, Composite Structures 204 (2018) 388 – 394. doi:https://doi.org/10.1016/j.compstruct.2018.07.055.

[17] B. Zuanetti, T. Wang, V. Prakash, A novel approach for plate impact experiments to determine the dynamic behavior of materials under extreme conditions, Journal of Dynamic Behavior of Materials 3 (1) (2017) 64–75.

[18] D. Grady, Shock-wave compression of brittle solids, Mechanics of Materials 29 (3-4) (1998) 181–203.

[19] J. R. Barber, Elasticity, Springer, 2009.

[20] A. Cohen, Numerical Methods for Laplace Transform Inversion, Springer, 2007.

[21] L. Brančík, Programs for fast numerical inversion of Laplace transforms in MATLAB language environment, Proceedings of the 7th Conference MATLAB'99 (1999) 27–39.

[22] V. Adámek, F. Valeš, J. Červ, Numerical Laplace inversion in problems of elastodynamics: Comparison of four algorithms, Advances in Engineering Software 113 (2017) 120–129.

[23] T. J. R. Hughes, The Finite Element Method: Linear Static and Dynamic Finite Element Analysis, Dover Publication, 2000.

[24] T. Belytschko, W. E. Bachrach, Efficient implementation of quadrilaterals with high coarse-mesh accuracy, Computer Methods in Applied Mechanics and Engineering 54 (3) (1986) 279–301. doi:10.1016/0045-7825(86)90107-6.

[25] R. Kolman, J. Plešek, J. Červ, M. Okrouhlík, P. Pařík, Temporal-spatial dispersion and stability analysis of finite element method in explicit elastodynamics, International Journal for Numerical Methods in Engineering 106 (2) (2016) 113–128. doi:10.1002/nme.5010.

[26] T. Belytschko, W. Liu, B. Moran, K. Elkhodary, Nonlinear Finite Elements for Continua and Structures, Wiley, 2013.

[27] O. Zienkiewicz, J. Zhu, The superconvergent patch recovery (SPR) and adaptive finite element refinement, Computer Methods in Applied Mechanics and Engineering 101 (1) (1992) 207 – 224. doi:https://doi.org/10.1016/0045-7825(92)90023-D.

[28] V. Guinot, Godunov-type Schemes: An Introduction for Engineers, Elsevier, 2003.

[29] R. J. LeVeque, Finite Volume Methods for Hyperbolic Problems, Cambridge University Press, 2002.

[30] P. L. Roe, Approximate Riemann solvers, parameter vectors, and difference schemes, Journal of Computational Physics 43 (2) (1981) 357–372.

[31] E. F. Toro, Riemann Solvers and Numerical Methods for Fluid Dynamics: A Practical Introduction, Springer Science & Business Media, 1997.

[32] E. F. Toro, Godunov Methods: Theory and Applications, Springer Science & Business Media, 2001.

[33] A. Berezovski, J. Engelbrecht, G. A. Maugin, Numerical Simulation of Waves and Fronts in Inhomogeneous Solids, World Scientific Singapore, 2008.